crystals

MDPI

Article

Insights in the Structural Hierarchy of Statically Crystallized Palm Oil

Fien De Witte [1,*], Ivana A. Penagos [1], Kato Rondou [1], Kim Moens [1], Benny Lewille [1], Daylan A. Tzompa-Sosa [1], Davy Van de Walle [1], Filip Van Bockstaele [1], Andre G. Skirtach [2] and Koen Dewettinck [1]

[1] Food Structure & Function Research Group, Department Food Technology, Safety and Health, Ghent University, Coupure Links 653, 9000 Ghent, Belgium
[2] Nano-Biotechnology Laboratory, Department of Biotechnology, Faculty of Bioscience Engineering, Ghent University, Proeftuinstraat 86, 9000 Ghent, Belgium
* Correspondence: fien.dewitte@ugent.be

Abstract: Palm oil (PO) is still widely used for the production of all types of food products. Due to its triacylglycerol (TG) composition, PO is semisolid at ambient temperature, offering possibilities for many applications. In order to tailor the fat crystal network for certain applications, it remains imperative to understand the structural build-up of the fat crystal network at the full-length scale and to understand the effect of processing conditions. In this study, PO was crystallized under four temperature protocols (fast (FC) or slow (SC) cooling to 20 °C or 25 °C) and was followed for one hour of isothermal time. A broad toolbox was used to fundamentally unravel the structural build-up of the fat crystal network at different length scales. Wide-angle and small-angle X-ray scattering (WAXS and SAXS) showed transitions from α-2L to β′-2L over time. Despite the presence of the same polymorphic form (β′), chain length structure (2L), and domain size, ultra-small-angle X-ray scattering (USAXS) showed clear differences in the mesoscale. For all samples, the lamellar organization was confirmed. Both cooling speed and isothermal temperature were found to affect the size of the crystal nanoplatelets (CNPs), where the highest cooling speed and lowest isothermal temperature (FC and 20 °C) created the smallest CNPs. The microstructure was visualized with polarized light microscopy (PLM) and cryo-scanning electron microscopy (cryo-SEM), showing clear differences in crystallite size, clustering, and network morphology. Raman spectroscopy was applied to confirm differences in triglyceride distribution in the fat crystal network. This study shows that both cooling rate and isothermal temperature affect the fat crystal network formed, especially at the meso- and microscale.

Keywords: palm oil; crystallization; X-ray scattering; WAXS; SAXS; USAXS; microscopy; Raman spectroscopy

Citation: De Witte, F.; Penagos, I.A.; Rondou, K.; Moens, K.; Lewille, B.; Tzompa-Sosa, D.A.; Van de Walle, D.; Van Bockstaele, F.; Skirtach, A.G.; Dewettinck, K. Insights in the Structural Hierarchy of Statically Crystallized Palm Oil. *Crystals* **2024**, *14*, 142. https://doi.org/10.3390/cryst14020142

Academic Editor: Borislav Angelov

Received: 20 December 2023
Revised: 25 January 2024
Accepted: 26 January 2024
Published: 30 January 2024

1. Introduction

Over the years, PO has become an incredibly popular fat for the production of food products, like margarines, shortenings, confectionary products, and frying oils [1]. PO contains almost equal amounts of saturated (myristic, palmitic, and stearic acid) and unsaturated (oleic and linoleic acid) fatty acids. Compared to other vegetable oils, PO is richer in saturated fatty acids, making it semisolid at ambient temperature. A certain amount of solid fat and the presence of a fat crystal network are often necessary to create a food product that is technologically, sensorially, and nutritionally functional. In order to control the macroscopic fat properties, a thorough understanding of the distinct structural levels of the fat crystal network (nanoscale: 0.1 nm–100 nm; mesoscale: 100 nm–1 µm; microscale: 1 µm–200 µm; macroscale: >200 µm) is a prerequisite [2].

Crystallization is the combined result of nucleation and crystal growth and is largely depending on the degree of supercooling [3]. At the nanoscale, the polymorphic form

(subcell) of the triacylglycerols (TGs) is of interest. Fundamentally, three polymorphs exist: α (hexagonal), β′ (triclinic), and β (orthorhombic) (from low to high stability and melting point). Polymorphic behavior is related to the TG composition of fat. More specifically, for PO, the polymorphic tendency depends on the content of palmitic acid, the ratio of palmitic to stearic acid, and the distribution of the fatty acids over the TGs (monoacid vs. mixed acid) [4–6]. Unlike the β preferential polymorphic tendency of pure tripalmitin (PPP), the preferential polymorphic tendency of PO is β′ [7]. Next to the sensu stricto polymorphism, TGs form lamellae, in which they adopt a two-chain (2L) or three-chain (3L) stacking, mainly depending on their fatty acid (FA) composition. Lamellae stack on top of each other and form crystal nanoplatelets (CNPs), of which the thickness is often called the 'domain' [8,9]. The network hierarchy proposed by Tang and Marangoni (2006) and Mishra et al. (2023) shows that CNPs arrange themselves into brick-like crystallites that group themselves in an asterisk-like structure, either fanning out from a central point [10] or more randomly attached from their sides [9], forming clusters. Several clusters group together into spherical structures, called flocs. Aggregation of these flocs results in a solid fat crystal network that can entrap liquid oil.

Known for its complex and specific crystallization behavior, PO has been a topic of interest for many studies over the years [11]. PO is prone to recrystallization during storage, which might lead to the formation of undesirable granular crystals [12,13]. Although this shows the need to study the formation of the fat crystal network on the nano-, meso- and microscale, the different scales are seldom combined. De Graef (2009) focussed on the microstructure of the fat crystal network under static and sheared conditions, using polarized light microscopy and confocal laser scanning microscopy. Crystallization at 18, 20, 22, and 25 °C was followed by pNMR, DSC, and time-resolved synchrotron XRD, showing that different polymorphic trajectories were followed and different microstructural networks were created [14]. Sainlaud et al. (2022) studied the static crystallization of palm oil using wide- and small-angle X-ray scattering (WAXS and SAXS). Lab-scale equipment was used, making time-resolved analysis difficult and forcing the author to use very slow cooling rates (0.08 to 0.5 °C/min). Application of the Scherrer formula showed that domain sizes increased by applying a slower cooling rate and a lower isothermal temperature (−5, 5, 15, and 25 °C) [7].

Until today, the mesoscale of fat crystal networks has only scarcely been studied. Peyronel and Pink have put substantial efforts into studying various fat systems, ranging from pure TGs and TG mixtures to plain fats and even chocolate [15–18]. Peyronel stresses the importance of understanding the mesoscale structure and its relation with the macroscopic properties. The relation between polymorphic form and the mesoscale structure has been tackled, showing that fats crystallized in the same polymorphic form can show different mesoscale behavior and that fats with similar mesoscale behavior can possess a different polymorphism. Nikolaeva et al. (2018) applied USAXS to study the network formation of micronized fat samples [19]. Rondou et al. (2022) applied USAXS to study the stability of monoglyceride oleogels [2]. So far, focus has been put on the mesoscale of stable crystallized fats and finished food products and not on the relation between processing conditions and the development and evolution of the mesoscale and the full-fat crystal network during crystallization.

In this study, PO was cooled at 1 °C/min (slow cooling) or 20 °C/min (fast cooling) and crystallized isothermally at 20 or 25 °C for 1 h. Various microscopic techniques (PLM, cryo-SEM, TEM, and Raman spectroscopy) were used to visualize the meso- and microstructure. Synchrotron and lab-scale X-ray scattering (XRS) were used to unravel the structural build-up of the fat crystal network on the nano- and mesoscale. Lab-scale SAXS was applied to study the lamellar stacking evolution during crystallization and the domain size after one hour of isothermal crystallization. Synchrotron radiation (WAXS/USAXS) allowed us to follow crystallization in detail over time, even at high cooling rates of 20 °C/min. This simultaneous USAXS and WAXS analysis provided insights into the CNP evolution, coupled to the polymorphic behavior of PO.

2. Materials and Methods

2.1. Palm Oil

Refined palm oil (PO) was kindly provided by Vandemoortele (Izegem, Belgium). The solid fat content was 48.1%, 34.2%, 19.3%, 10.1%, 5.4%, and 2.8% at 10 °C, 15 °C, 20 °C, 25 °C, 30 °C, and 35 °C, respectively.

2.2. Temperature Protocols

In order to assess the effect of cooling rate (slow cooling at 1 °C/min or fast cooling at 20 °C/min) and isothermal crystallization temperature (20 or 25 °C), different temperature protocols were applied. The samples were first heated at 70 °C for 10 min to erase crystal memory, cooled at 1 °C/min or 20 °C/min to 20 °C or 25 °C, and then kept isothermally for 60 min at 20 °C or 25 °C. These temperature protocols were applied to describe the crystallization behavior of PO using the techniques described below.

2.3. Thermal Behavior by Differential Scanning Calorimetry

Differential scanning calorimetry (DSC) was used to analyze the crystallization and melting behavior of PO. PO (5–15 mg) was added to aluminum pans (TA Instruments, Zellik, Belgium). Pans were hermetically sealed using a pan crimper. The DSC equipment (Q1000, TA Instruments, New Castle, DE, USA) was calibrated using indium, azobenzene, and undecane. An empty pan was used as a reference. Each analysis was performed in triplicate.

To characterize the crystallization/melting behavior of PO, PO was crystallized/melted at different cooling/heating rates. The following method was used: equilibration at 70 °C, 10 min isothermal hold, temperature decrease until −50 °C at a rate of 1, 5, 10, 20, or 30 °C/min, isothermal hold for 1 min, and temperature increase until 70 °C at a rate of 1, 5, 10, 20, or 30 °C/min. The crystallization and melting behavior were assessed by differential scanning calorimetry (DSC) and can be found in Figure A1 (Appendix A).

2.4. Crystallization and Melting Behavior by Differential Scanning Calorimetry

Time-resolved crystallization was mimicked using DSC (setup described above) by applying the four temperature protocols specified above.

2.5. Microscale

2.5.1. Crystal Floc Morphology by Polarized Light Microscopy

Crystallization over time was followed with a polarized light microscope, Leica DM2500 (Leica, Wetzlar, Germany), equipped with a 20× magnification lens (type HC PL Fluotar, dry, NA 0.5). PO was put between a microscope slide and a cover glass. The PE120 Peltier stage (Linkam, Redhill, UK) was programmed according to the temperature protocols specified above. Leica Application Suite (LAS) software was used to obtain the pictures. Measurements of crystal floc diameters were made using ImageJ software, and the number of replicates (N) was specified with the measurements.

2.5.2. Spatial Distribution of Triglycerides by Raman Spectroscopy

PO was crystallized on a non-covered microscope slide using the PE120 Peltier system, after which the sample was transferred to an isothermal cabinet at the respective crystallization temperature until the analysis 1 week later. Raman spectroscopy was performed on the microscope slide with a WITec alpha 300 microscope (Oxford Instruments, Abingdon, UK) coupled to a XTRA II laser diode (wavelength 785 nm, TOPTICA Photonics, Gräfelfing, Germany). The spectrometer used was a UHTS 300 (Oxford Instruments), equipped with a CCD camera cooled at −60 °C (ANDOR iDus 401 BR-DD, DU401A-BR-DD-352, Oxford Instruments). WITec Control FIVE was used as operational software. For the data acquisition, a 40× objective (CFI S Plan Fluor ELWD 40×, NA 0.6, Nikon, Tokyo, Japan) was used, the laser was set at 54 mW, and 300 gratings with a spectral center of 2000 were used. In every sample, an area of 80 µm × 80 µm was mapped to derive the spatial distribution of

the triglycerides. The spectrum was obtained every 1 µm (for FC-25) or 2 µm (for FC-20, SC-20, and SC-25), with an acquisition time of 0.5 s. Using Project FIVE software, data were corrected for cosmic rays, and a background of shape 1000 was subtracted. To produce the heatmaps, the Raman spectra were first normalized by intensity. Per scanning point, the minimal intensity was subtracted, after which all intensities were divided by the maximum intensity in that spectrum. After this, a certain Raman shift (1654 cm^{-1} or 1127 cm^{-1}) was selected. The normalized intensity was scaled by subtracting the minimum normalized intensity per area. This value was plotted for every scanning point. A single spectrum of 0.5 s of the pure triglyceride tripalmitin (PPP) was obtained to select the Raman shift corresponding to solid fat.

2.5.3. Floc and Crystallite Morphology by Cryo-Scanning Electron Microscopy

A small amount of PO (0.25 g) was crystallized on a microscope slide without cover glass using the PE120 Peltier system. After crystallization, PO was put into pre-tempered centrifuge tubes. The oil was extracted from the sample by adding 15 mL of pre-tempered isobutanol and shaking the suspension. The top layer of isobutanol containing the oil was removed, and a fresh solvent was added. This procedure was repeated daily for 3 subsequent days.

The extracted crystalline fat was visualized using cryo-SEM (JEOL JSM 7100F; JEOL Ltd., Tokyo, Japan) on the fourth day after the crystallization of the sample. A droplet of the fat suspended in isobutanol was put on an aluminum stub covered with carbon tape, after which the isobutanol was allowed to evaporate overnight. The stubs were vitrified in a nitrogen slush and transferred under vacuum conditions into the cryo-preparation chamber (PP3010T Cryo-SEM Preparation System, Quorum Technologies, Lewes, UK) conditioned at −140 °C. Subsequently, the sample was sublimated for 45 min at −70 °C, sputter-coated with platinum using argon gas for 90 s, transferred to the SEM stage at −140 °C, and electron beam targeted at 3 keV.

2.5.4. Triglyceride Analysis of Palm Oil and Extracted Samples

Triglyceride analysis was performed by means of high-pressure liquid chromatography (Binary pump 1525 and autosampler 2707, Waters Corporation, Milford, MA, USA) coupled to Refractive Index detector (model 2414, Waters) according to method AOCS Ce 5b-89. This allows triacylglycerol separation according to equivalent carbon number. The fat samples were melted and put in a solution of 1:4 chloroform:iso-octane. A total of 10 µL of the mixture was injected in a LiChrospher 100 RP-18 5 µ (250 mm × 4.0 mm) column (Merck KGaA, Darmstadt, Germany) at 30 °C. A mixture of aceton and acetonitrile (60/40) was used as the mobile phase. Data analysis was performed using Empower software (Waters Corporation, Milford, MA, USA).

2.6. Nano- and Mesoscale

2.6.1. Crystal Nanoplatelet Visualization by Transmission Electron Microscopy

For FC-20, the isobutanol-extracted crystalline fat was visualized using TEM (JEOL JEM 2200-FS; JEOL Ltd., Tokyo, Japan) equipped with an EM21090 cryo-holder. The sample was placed on a TEM grid of 200 mesh (Electron Microscopy Sciences, Hatfield, PA, USA) coated with Formvar, and excess liquid was blotted for 2 s using filter paper. A staining aqueous solution of 2% uranyl acetate was used to enhance contrast for 10 s, and excess liquid was blotted again for 2 s using filter paper. The grid was air dried overnight, after which it was visualized.

2.6.2. Crystal Nanoplatelet Morphology and Size by Ultra-Small-Angle X-ray Scattering and Polymorphism by Wide-Angle X-ray Scattering

Crystal nanoplatelet size and morphology and polymorphism were obtained by measuring simultaneous USAXS/WAXS profiles on the TRUSAXS instrument of the European Synchrotron Radiation Facility (ID02 ESRF, Grenoble, France) using a photon en-

ergy of 12.230 keV and at a sample-to-detector distance of 31 m. The detector used for USAXS was the EIGER2-4M, on which the range of the scattering vector (q) was $0.0002\ Å^{-1} < q < 0.02\ Å^{-1}$. The WAXS detector used was a Rayonix LX-170HS, which was located on the top of the cone of the 34 m evacuated USAXS tube. The q-range recorded on this detector was $0.7\ Å^{-1} < q < 3.7\ Å^{-1}$. The beamline setup is described in detail by Narayanan et al. (2022) [20].

The fat sample was put in quartz glass capillaries of 1.5 mm in diameter (WJM-Glas, Berlin, Germany) and left unsealed. The temperature protocols specified above were applied using a Linkam THMS600 stage (Linkam, Redhill, UK). For each acquisition, 10 shots were taken and averaged. The exposure time was set to 0.02 s, resulting in 17 s time between 2 acquisitions. For the last 30 min of isothermal time, acquisitions were only collected every 5 min. From each of the USAXS profiles, the background of the capillary filled with the liquid oil was subtracted, as it was aimed to measure the scattering coming from the solid fat. USAXS data were plotted against q in three ways: (1) intensity I as a function of scattering vector q: I(q), (2) $I \times q^2(q)$ (Kratky plot), and (3) $I \times q^4(q)$ (Porod plot) to aid in the visual assessment of the data. The slopes at low and high q were fitted in the range of $0.0007\ Å^{-1} < q < 0.002\ Å^{-1}$ and $0.006\ Å^{-1} < q < 0.02\ Å^{-1}$, respectively. The lowest q value for which the I(q) curve is straight and accords to the slope at high q will be called the cut-off point. To determine the cut-off point, the fit in the range of $0.006\ Å^{-1} < q < 0.02\ Å^{-1}$ was extrapolated over the full q-range, and the difference with I(q) was determined. The cut-off point was defined as the point where the deviation was at zero, before the I(q) bends back and deviation starts to increase continuously. WAXS data were corrected by the subtraction of an empty capillary. The polymorphic form over time was derived via a comparison of peak positions to existing literature.

2.6.3. Lamellar Spacing, Average CNP Thickness, and Thickness Distribution by Small-Angle X-ray Scattering

Time-resolved SAXS data were collected on a Xeuss 3.0 system (Grenoble, France), equipped with an Eiger2R 1M detector from Dectris (Baden, Switzerland) and a Cu-source Genix 3D form Xenocs (Grenoble, France), providing a wavelength of 1.54 Å. Voltage and current were 50 kV and 0.60 mA, respectively. Quartz capillaries of 1.5 mm in diameter (WJM-Glas, Berlin, Germany) were filled with PO, sealed, and put into a Linkam THMS600 heating/cooling stage, equipped with a liquid nitrogen Dewar and programmed with each of the temperature profiles. SAXS data were acquired with a sample-to-detector distance of 360 mm, resulting in $0.05\ Å^{-1} < q < 0.65\ Å^{-1}$. The acquisition time was set at 60 s; the total time between 2 subsequent measurements was 70 s due to a cosmic background correction and the calculation of absolute intensity. SAXS data were corrected by the subtraction of the profile of an empty capillary.

From the SAXS data, different parameters were obtained. The reported values were obtained at the end of one-hour crystallization. In this case, the results from the last three profiles (70 s apart) are averaged. First, the lamellar spacing (d_{001}) was derived from the position (q_{001}) of the first-order (001) crystallization peak following Equation (1):

$$d_{001} = \frac{2 \times \pi}{q_{001}} \quad (1)$$

Secondly, the full width at half maximum (FWHM) from the first-order (001) crystallization peak was obtained. The Scherrer equation was applied to derive the thickness τ (domain) of the nanoplatelet (Equation (2)) and thus the number of lamellae stacked on top of each other [21,22]:

$$\tau = \frac{K \times \lambda}{\beta \times \cos\theta} \quad (2)$$

where K is a numerical constant with a value close to 1. In this research, a factor of 0.9 was applied since it is often used for platelets [23]. λ is the wavelength, β is the FWHM

(radians), and θ is the Bragg angle (radians). These data were not corrected for instrumental broadening, as the goal was only the compare between samples.

Thirdly, the Bertaut–Warren–Averbach method (BWA) was applied to obtain the CNP thickness distribution by taking into account the full SAXS peak shape as described in den Adel et al. (2018) [24]. The method of Rondou et al. (2022) was optimized by fitting the SAXS peak with a Gaussian of multiple terms [2]. Within the range of $-0.5 < s^* < 0.5$, 15 equally spaced peaks were used. As such, it was no longer assumed that the distribution of the CNP thicknesses is Gaussian but rather that it consists of a multimodal distribution, which has been suggested by the results of Acevedo and Marangoni (2010) and Ramel et al. (2016) [23,25].

2.7. Graphs and Statistics

Data were recorded by programs specifically adapted for the device used, as mentioned above. All graphs were produced using Matlab R2023a. If relevant, statistics were performed with SPSS Statistics 29 (SPSS Inc., Chicago, IL, USA). Means were compared utilizing a one-way ANOVA test. The condition of homogeneity of variances was checked by means of a Levene test. A Tukey test was used if variances were homogeneous. Otherwise, Dunnett's T3 test was preferred. Each test was performed at a 5% significance level.

3. Results and Discussion

3.1. Microscale

3.1.1. PLM

PLM was used to visualize the microstructure of the fat crystal network during crystallization (Figure A2, Appendix A). The 20× magnification, allowing us to clearly visualize structures in 2D, was down to about 10 µm. When fast cooling PO to 20 °C, the crystallization started when the temperature approached 20 °C. A similar timing was found using DSC (Figure A3, Appendix A). Due to the high cooling rate, many nucleation sites were formed, resulting in small crystal flocs and a high crystallization rate (Figure A2, Appendix A) [26]. The PLM image obtained is similar to the one of De Graef et al. (2009), and they used a cooling rate of 10 °C/min [14]. No changes occurred after 7.5 min. The average crystal diameter after one hour of isothermal time was 19.5 ± 3.5 µm (Figure 1A, Table 1).

Table 1. Image J measurements of the largest width of fat crystals as found by PLM after one hour of crystallization at 20 or 25 °C. N indicates the number of measurements. Superscripts a to c indicate a significant change from bigger to smaller.

Sample	Abbreviation	Min (µm)	Max (µm)	Average (µm)	N
Fast cooled (20 °C/min) to 20 °C	FC-20	12.3	30.1	19.5 ± 3.5 ^{c}	70
Slow cooled (1 °C/min) to 20 °C	SC-20	21.5	70.8	46.2 ± 10.5 ^{b}	80
Fast cooled (20 °C/min) to 25 °C	FC-25	37.9	117.2	69.9 ± 18.0 ^{a}	27
Slow cooled (1 °C/min) to 25 °C	SC-25	21.4	138.2	75.5 ± 27.6 ^{a}	104

PO slowly cooled to 20 °C and started crystallizing as large snowflake-like crystal flocs before reaching 20 °C (after 48 min). The number of flocs is lower compared to FC-20. Over time, the number did not increase, but it seemed to expand slightly from 65 min onwards (Figure A2, Appendix A). After one hour of isothermal time, an average size of 46.2 ± 10.5 µm was observed (Table 1, Figure 1D). The PLM results of Smith et al. (2022) obtained at 23 °C also show a network similar to the ones found here at 20 °C. The size is somewhere in between FC-20 and SC-20, which can be explained by the non-controlled cooling rate used by these authors [27].

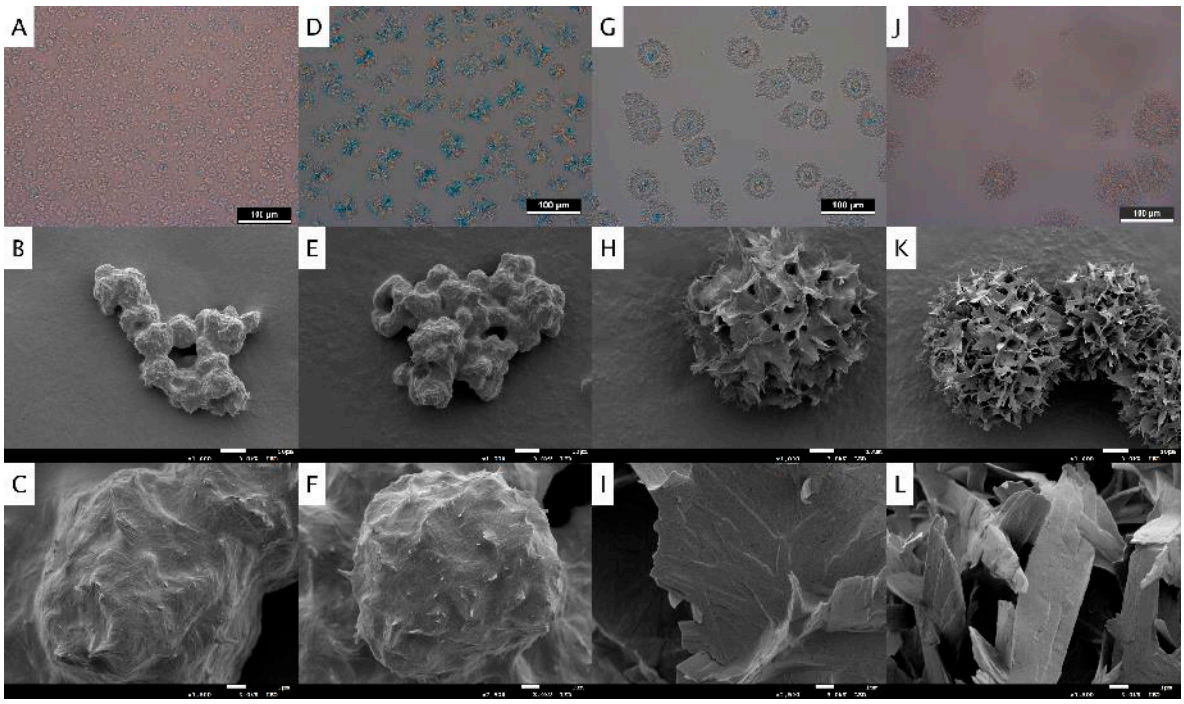

Figure 1. Upper row: polarized light microscopy images after one hour of isothermal crystallization. Middle and lower row: cryo-SEM images of de-oiled fat samples at magnifications of ×1000 (top, scale bar = 10 µm) and ×7500 (bottom, scale bar = 1 µm). Picture (**A**–**C**) shows FC-20, (**D**–**F**) SC-20, (**G**–**I**) FC-25, and (**J**–**L**) SC-25. Sample abbreviations can be found in Table 1.

On the contrary, when fast cooling to 25 °C, the first crystals were only formed after 7 min (supported by DSC, Figure A3, Appendix A), and the number of nuclei, and consequently, the number of crystal flocs, were lower at the beginning but kept increasing for some time (until about 10 min). Initially, the spherical crystals were dense, but further during the isothermal time they expanded outwards with a less dense crown. This fanning crown expanded until one hour of isothermal time, yielding flocs with an average diameter of about 69.9 ± 18.0 µm (Figure 1G, Table 1). It remained possible to distinguish the center of the crystal from the outer part. The different flocs appeared separately and did not seem to form a network. A similar observation was made by Chen et al. (2002), although their setup included a high shear rate. The authors discussed that first the spherical crystal is formed in the α polymorph, after which needle-like crystals in the β′ polymorph fully surround the spherical crystals. However, in the study by Chen et al. (2002), the applied X-ray diffraction could not elucidate if the α crystals remained to exist and were invisible due to the surrounding β′ crystals or that the center of the crystals kept a spherical shape but was transformed into the β′ polymorph [28].

Slow cooling to 25 °C resulted in flocs with a formation and appearance similar to FC-25 °C, including a dense center (Figure 1J). A similar result was obtained by De Graef (2009), cooling at 10 °C/min [14]. PLM images suggest that the lower cooling rate results in less fat getting crystallized. For all samples, the PLM images suggest only very little interaction between the different flocs of a sample and no full network formation. However, this might be only a feature derived from the crystallization between two glass plates and the focus on one plane.

In general, the microstructure formed was affected by both the cooling rate and the isothermal temperature. A lower cooling rate and a higher isothermal temperature resulted in the formation of coarser flocs. Herrera and Hartel (2000) demonstrated for milk fat that both a lower cooling rate and higher isothermal temperature result in a coarser network with a wider crystal size distribution [29]. Campos et al. (2002) discussed that coarser flocs have weaker interactions, which results in the formation of a softer fat sample. Amongst

other things, the size of the fat crystals is related to the functionality of the fat crystal network: oil holding capacity, creaming, and plasticity [30]. The goal of this paper is, however, not to characterize the microscale but to understand how the nano- and mesoscale contribute to the formation of different microscales. As such, this study aims to give insights into the nano- and microscale.

3.1.2. Cryo-SEM

Cryo-SEM allowed surface visualization of the flocs, clusters, and crystallites and their relative positioning (Figure 1B,C,E,F,H,I,K,L). It provides more insight into the 3D structure compared to PLM. Nevertheless, cryo-SEM visualization requires the oil to be extracted from the sample, implying that the sample can be manipulated. In contrast to the methods proposed by Acevedo and Marangoni (2010) [23] and Ramel et al. (2016) [25], no shear or sonication was applied during the oil extraction process in order to maintain the fat crystal network as much as possible. Two possible problems when de-oiling with isobutanol have been described by Chawla et al. (1990): (1) the dissolution of the solid fat phase and (2) the retention of the oil phase [31]. Although the authors describe the dissolution or retention not to be >5%, it cannot be ruled out that the current samples were altered by de-oiling. An overall structure consisting of small, irregularly shaped balls attached to each other was seen in FC-20 (Figure 1B). Taking into account the floc size found with PLM (12 to 30 µm diameter, Table 1), this appears to be consistent with the network view, as visualized by cryo-SEM. Magnification (7500×, Figure 1C) shows a rather smooth surface where some randomly oriented crystallites of approximately 1 µm length can be distinguished. This serves only as a rough size indication, as cryo-SEM is a surface visualization technique and is thus not well-suited to estimate sizes. It is possible that the surface was smoothened due to the de-oiling procedure.

For slowly cooled PO (SC-20), a structure similar to FC-20 was obtained with cryo-SEM (Figure 1E). Nonetheless, the shape is more irregular, and the different flocs appear more entangled with each other. The bigger size seems consistent with PLM. When looking at higher magnifications, it can also be seen that the surface of the flocs appeared less smooth compared to FC-20 (Figure 1F), which is consistent with the PLM results. The crystallite length seems similar to FC-20 or slightly larger.

For FC-25, the lowest magnification (1000×, Figure 1H) shows only one floc with an approximate size of 80 µm, which is in the range of 38–117 µm, as found by PLM (Table 1). No other flocs were found attached to it. This might be related to the de-oiling procedure applied. The 7500× magnification (Figure 1I) provides a view of the crystallites that build up the floc. It is clear that oil has been removed from between the clusters, resulting in a non-dense structure, which is consistent with the fanning crown seen by PLM (Figure 1G). The positioning of the crystallites is not random but rather starts from a central point within the cluster. The crystallites join on one side and fan out toward the other side, resulting in a petal-like structure. The petals seem to be present randomly over the floc. The crystallites appear to be coarser than for FC-20 and SC-20. For SC-25, the 1000× cryo-SEM image (Figure 1K) shows flocs that look similar to the FC-25 floc. At a higher magnification (Figure 1K), the crystallites show a more random orientation on the surface, which might be related to the de-oiling protocol.

3.1.3. Triglyceride Analysis

In order to investigate the effect of the de-oiling protocol, the TG content of the solid fat samples (FC-20, SC-20, FC-25, SC-25) after oil extraction was determined. Figure A4 (Appendix A) shows that all samples were enriched in dipalmitoyl-myristoyl-glycerol, tripalmitoyl-glycerol, dipalmitoyl-stearoyl-glycerol, and distearoyl-palmitoyl-glycerol (MPP, PPP, PPS, and PSS) and were all trisaturated TGs with a high melting point [32]. The enrichment in PPP from 5.4% to over 60% for all samples proves that a large fraction of the solid material was retained. All TGs taking part in the liquid fraction were clearly diminished in concentration; all OOO was virtually removed. We should, however, take

into consideration that the treatment with isobutanol might have dissolved some of the TGs present in the solid fat crystal network.

A discrepancy was found between the remaining TGs in the solid fraction of the different cooling protocols. Based on isothermal temperatures, we expected the samples isothermally crystallized at 20 °C (FC-20 and SC-20) to be richer in low-melting TG and thus to be relatively poorer in high-melting (saturated) TG compared to the samples crystallized at 25 °C. For example, for PPP, this is true within the same cooling rate: 68.6% PPP for FC-20 compared to 70.8% for FC-25 and 61.0% for SC-20 compared to 62.9% for SC-25. Additionally, the fast-cooled samples (FC-20 and FC-25) are a lot richer in PPP compared to the slow-cooled samples. A similar result was found for MPP, PPS, and PSS, although their concentration and thus the difference thereof is lower (Figure A4, Appendix A). This shows that the cooling rate, and thus the type and density of the crystal network formed, matter. Based on the results, it is hypothesized that the spatial arrangement of TGs is distinct based on the cooling protocol. Possibly, more PPP (and other saturated TGs) was included during the nucleation when the fast-cooling methods were applied. When a high cooling rate is applied, high-melting TGs will be undercooled rapidly. As a result, they crystallize in many nucleation points [33]. For FC-20, more nucleation sites were formed (Figure 1), whereas PPP (PPS, PSS, and other saturated TGs) will have been included as the central material. Similarly, for FC-25, the PLM images show big, dense centers, whereas PPP was probably strongly embedded centrally and was presumably less prone to extraction with isobutanol, resulting in a higher retention.

3.1.4. Raman Spectroscopy

Raman spectroscopy was applied to further characterize the floc centers found for FC-25 and SC-25. First, the profile of pure PPP was obtained as a reference (Figure A5, Appendix A). From these profiles and based on the literature, two characteristic Raman shifts were selected. Wavenumber 1127 cm^{-1} (C-C stretching/C-O-C vibration) was seen as characteristic for the saturated fraction (consisting mainly of PPP), while 1654 cm^{-1} (C=C stretching) was used to characterize the more unsaturated (and thus liquid) areas of the sample [34,35].

Figure 2 shows a light microscopy image of the samples with the selected Raman mapping area and the corresponding heatmaps filtered at 1127 and 1654 cm^{-1}. The microscopy images show a dense network for FC-20 and SC-20, while clearly separate flocs are seen for FC-25 and SC-25. The Raman heatmaps clearly reveal the solid network from the liquid oil. Neither for FC-20 nor for SC-20 concentrated kernels were found. Contrarily, three different zones exist within the sample for FC-25 (Figure 2). In the most central zone, a small core is present, strongly responding to the PPP-related bands. This is in correspondence with the centers seen by PLM and with the hypothesis of the PPP being maintained in the centers of the floc during de-oiling. The largest area of the floc surrounding the center shows medium intensity for both liquid and solid wavenumbers. Next to PPP, this area probably also contains dipalmitoyl-oleoyl-glycerol (PPO), for example. The last area comprises the outer part of the fanning crown. Although seen as part of the floc and thus the crystalline material of the fat, it almost fully responds to the liquid Raman signal. This is expected, as the scanning step size of the Raman scanning is rather large (1 or 2 µm) and the crystallites are positioned quite spaciously toward each other, holding oil in between them (see Figure 1). The profiles found for SC-25 resemble those of FC-25, where clear floc structures, including a saturated center, can be distinguished from the surrounding oil. A similar morphology was found when crystallizing POP:OPO mixtures in a 75:25 ratio. Bayés-García et al. (2011) showed by means of synchrotron microbeam X-ray diffraction that the inner floc center differed in composition with the fanning crown (the center consisted of a mixed crystal, while the outer parts were purer in POP) [6].

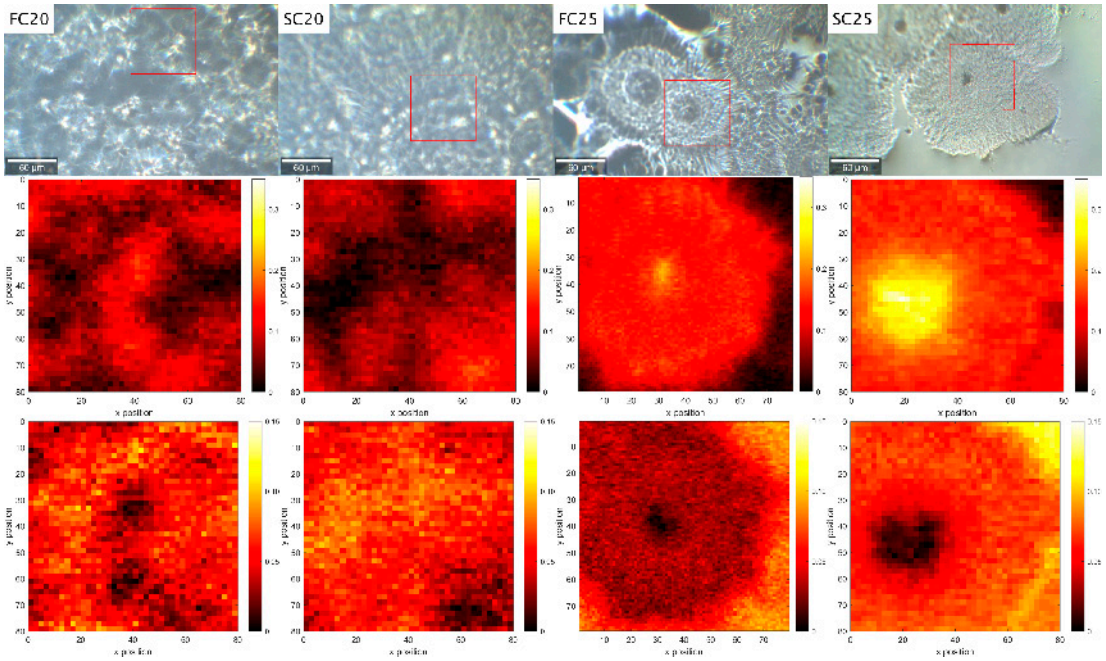

Figure 2. From left to right: FC-20, SC-20, FC-25, and SC-25. (**Top row**): Light microscopy images with an indication of the selected area (80 µm × 80 µm) for Raman spectroscopy mapping. (**Middle row**): Raman heatmaps for the selected area at 1127 cm^{-1}, indicative of the solid fat fraction. (**Lower row**): Raman heatmaps for the selected area at 1654 cm^{-1}, indicative of the oil fraction.

3.2. Nano- and Mesoscale

3.2.1. USAXS and WAXS

Although underexposed for many years, the importance of the mesoscale structure has recently gained more interest. USAXS is a technique that measures the electron density difference (contrast) present in the sample [36]. In low solid samples, the scattering is caused by the 'minority phase' referred to by Peyronel (2014) [37]. Within the PO samples, the contrast lies between the solid and liquid parts of the fat. The scattering is caused by the limited amount of solid fat in the majority of oil, providing structural information about the solid fat crystal network. USAXS data consist of straight and bent zones and are interpreted by fitting models to it [15,38]. This procedure is cumbersome, and data interpretation requires great caution. Over the years, the Unified Fit model has been applied the most. It relies on the fact that one structural level corresponds to the linear combination of one Porod power law region and one Guinier law bending section [39,40]. It assumes spherical scatterers, as spheres have only one characteristic dimension, which makes the interpretation of scattering at different levels more straightforward. It is, however, known from previous research with atomic force microscopy and TEM that CNPs are not spherical, but, as their name suggests, have a platelet-like shape [7,23,25,41]. To account for the scatterer shape, the Guinier–Porod model is sometimes applied. It has an extra parameter(s) called the 'shape factor', which serves to assess, within certain limits, the shape of a scatterer [38]. A limitation of this model is that it can only be used for dilute, monodisperse, and isotropic solutions of particles [42].

Some PO-based fat systems have been described by Peyronel et al. (2014) after fitting the nified Fit and Guinier–Porod model [37]. The systems were mostly stored for a prolonged time at 5 °C and crystallized with an unknown cooling rate. Varying values for the slopes at low and high q were found, as well as big differences in the radius of gyration for the CNPs and their aggregates and differences in the values for the shape parameter. Until today, USAXS has never been used to study fat crystallization over time. The application of simultaneous time-resolved WAXS and USAXS allowed us to study the mesoscale variations, coupled to the well-known polymorphic transitions. It has been

presented by Peyronel et al. (2014) that systems with similar polymorphic behavior can have different mesoscale behavior and vice versa [37].

For ease of explanation, five WAXS and USAXS frames were selected for every sample (Figure 3), specifically (1) the liquid sample at 70 °C (black), (2) the start of crystallization in the α polymorph (blue), (3) a pronounced α polymorph before polymorphic transition (green), (4) the β′ polymorph after polymorphic transition (pink), and (5) the end situation after one hour isothermal crystallization (red). Apart from the oil profiles, all profiles (2-3-4-5) were obtained after the isothermal temperature was reached. The data obtained comprise the range of 0.0003 $Å^{-1}$ < q < 0.02 $Å^{-1}$, implying that information is yielded about structures roughly between 30 nm and 2 µm in size. Taking into consideration the fat crystal networks proposed by Mishra (2023) and Tang and Marangoni (2006), this range allows us to detect CNPs and maybe their aggregates (crystallites) [9,10].

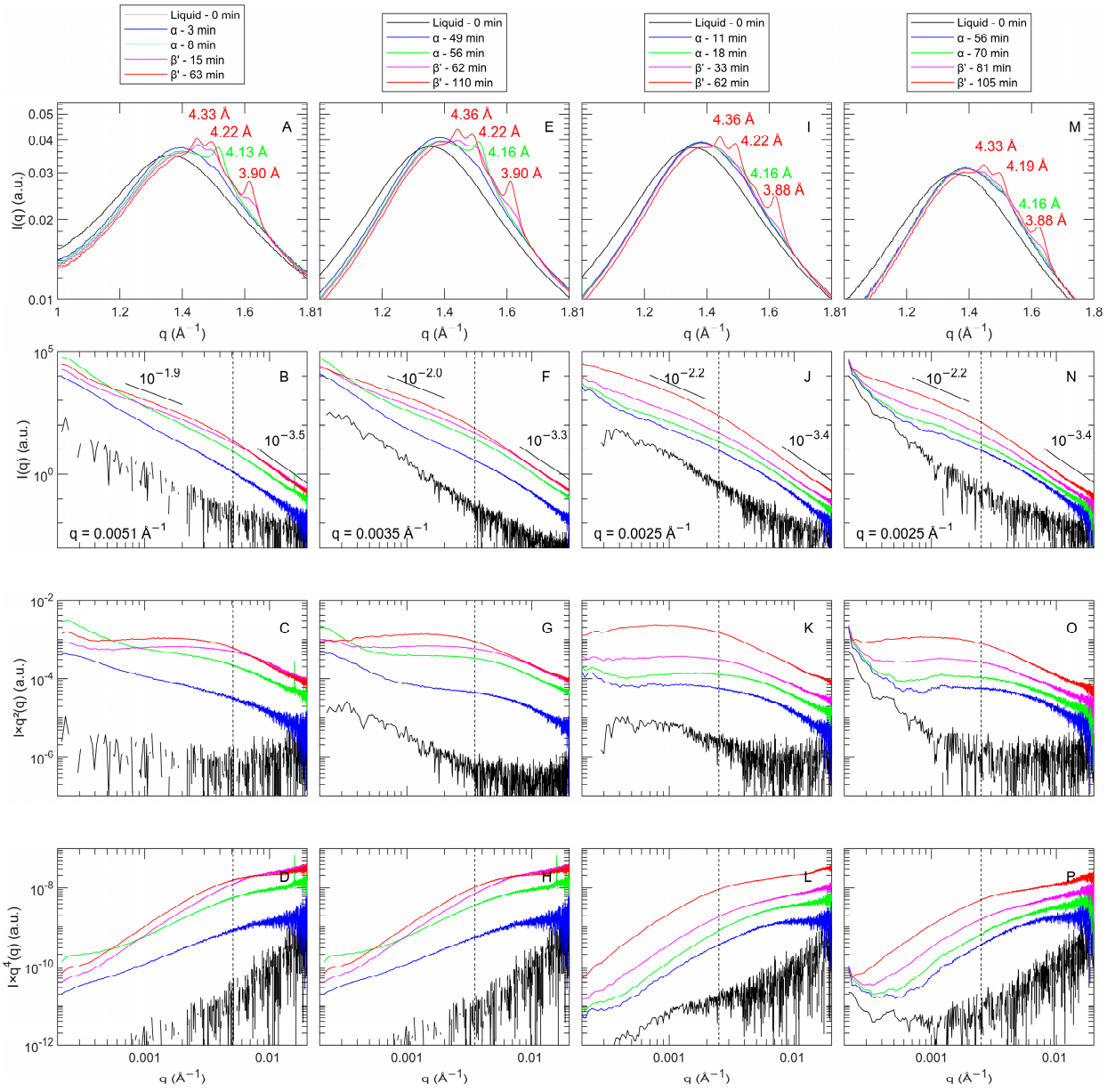

Figure 3. Overview of time-resolved WAXS and USAXS data. First row: WAXS I(q) data. Second row: USAXS I(q) data. Third row: USAXS I × q^2(q) data (Kratky plot). Fourth row: USAXS I × q^4(q) data. (**A**–**D**) for FC-20, (**E**–**H**) for SC-20, (**I**–**L**) for FC-25, and (**M**–**P**) for SC-25. The dotted lines represent the cut-off points after one hour of isothermal crystallization.

Oil is characterized in WAXS by a broad peak around q = 1.36 $Å^{-1}$ (Figure 3A,E,I,M, black). A slight change in the peak position toward q = 1.39 $Å^{-1}$ appeared when cooling is applied. Mazzanti et al. (2021) related the shift in the broad peak to the structuring of the liquid TGs [43]. In USAXS, the oil profiles obtained are dominated by noise caused by the subtraction protocol (Figure 3B,F,J,N, black; USAXS and WAXS). Upon cooling above the crystallization temperature, the intensity of the USAXS profile increased to a similar extent over the full q-range compared to the liquid baseline, removing the noise domination and creating a straight profile.

Fast Cooling of PO to 20 °C

For FC-20, a WAXS peak around q = 1.51 $Å^{-1}$ appeared at 20 °C (Figure 3A, blue), which is characteristic of the α polymorph [11]. The USAXS profile changes accordingly (Figure 3B, blue), and intensity increases in the right half of the profile, causing the profile to deviate from the straight baseline. As such, the profile is transformed from a straight line into an S-shaped curve, consisting of three straight parts joined by two bending sections. As the α polymorph is augmented (Figure 3A, green), the overall USAXS intensity increases, and the bending sections become more pronounced (Figure 3B, green).

From 8 min onwards, the WAXS profile showed a peak shift from q = 1.51 $Å^{-1}$ toward q = 1.45, 1.50, 1.56, and 1.62 $Å^{-1}$ (Figure 3A, pink), corresponding to the transition from an α to a β′ polymorph [44]. From 15 min onwards, the α to β′ polymorphic transition is finished. It is known that PO is a β′-tending fat due to the presence of asymmetric mixed-acid TGs, like POO and PPO, and that this polymorph results in the desired properties for many applications [3]. Figure A2 (Appendix A) reveals that the dense floc center on the microscale remains unchanged after the α to β′ polymorphic transition, as was also concluded by De Graef (2009) [14]. In USAXS (Figure 3B,C, pink), the intensity in the high q region increases, which is consistent with the further solidification of the sample. The bending section at high q becomes more pronounced and moves gently to a lower q position, implying that crystallization continues and CNP size increases. At lower q, the profile bends back, moving the bend toward lower q, which is consistent with the growth of the CNP aggregates.

After one hour of isothermal crystallization (Figure 3B, red), the interpretation of the final profile is made by separating the straight zones (one at low q and one at high q) from the bent zone. The straight lower q region is called the Porod region. On this length scale (>30 nm), the contrast comprises the interface between the liquid and the solid fat. This scattering region is supposed to behave according to the law of Porod with a theoretical decay to the power P = 4 for sharp interfaces [45]. The Porod plot ($I \times q^4(q)$, Figure 3D) illustrates the (dis)accordance with the law: any curve decaying to the power P = 4 will be shown as a horizontal line (at high q) on the Porod plot. For FC-20, the decay is found to be P = 3.5, which is close to 4 but deviates, probably because the contrast between liquid and solid fat is not well defined. In case a deviation of the 'ideal' Porod behavior is found, and the intensity varies with another power of q, a fractal interpretation is given. On the one hand, if a decay P > 3 is found, the object has a rough surface (surface fractal), and its fractal dimension is defined as $6 - |P|$. Mass fractals, on the other hand, show a P < 3, and their fractal dimension is given by P directly [45].

The middle q region comprises the bending section of the curve. The Kratky plot (Figure 3C) makes the bending section clearly visible: the bending section has the maximum intensity. It is the end of the Porod linear zone (cut-off point) that appears when CNPs are formed and that characterizes the overall size of the scatterers. The cut-off point is found at q if 0.0051 $Å^{-1}$ and illustrated by a dotted line. The straight zone toward lower q gives an indication of the shape of scatterers. A decay to the power of 1.9 results in a horizontal zone in the Kratky plot (Figure 3C), corresponding to a flat, lamellar-based shape [46]. This flat shape is confirmed by the TEM images in Figure 4 and is in accordance with the models proposed by Tang and Marangoni (2006) and Mishra et al. (2023), where aggregations of flat CNPs into crystallites were shown [9,10]. Taking into account the three different

dimensions of a platelet and the polydispersity thereof, it is impossible to give a simple value for its size, but a comparison of the samples is possible [46].

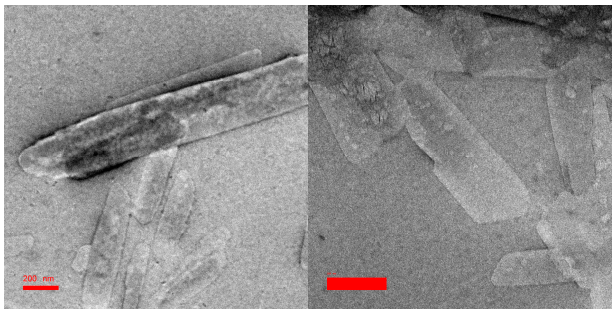

Figure 4. TEM images of de-oiled PO FC-20 showing CNPs and their aggregate (crystallite). Both scale bars represent 200 nm.

Apart from the two straight zones connected by a bending zone discussed above, the profile for FC-20 (Figure 3B, red) shows an extra straight and bent zone at very low q. The lowest q region can contain information about the aggregation (type and size) of the CNPs. Based on the cryo-SEM images, the crystallite size can indeed be below a few microns (Figure 1C) and was the smallest for all samples studied. Nonetheless, the q-range probed for this level (0.0003 to 0.0005 $Å^{-1}$) is too small to derive the slope of this zone and to interpret it further. As such, we cannot conclude with these USAXS results about the aggregation of the CNPs. Table 2 provides an overview of the parameters found after one hour of isothermal crystallization.

Table 2. Overview of parameters obtained from SAXS and USAXS analysis. Superscript a indicates that no significant differences were found for the different samples per parameter.

Sample	SAXS				USAXS		
	Polymorph and Chain Length Structure	d_{001} (Å)	Scherrer Average Number Lamella (-)	BWA Average Number Lamella (-)	Slope Low q (-)	Cut-Off Point ($Å^{-1}$)	Slope High q (-)
FC-20	β′-2L	42.1 ± 0 [a]	12.0 ± 0.1 [a]	10.1 ± 0.1 [a]	1.9	0.0046	3.5
SC-20	β′-2L	42.1 ± 0 [a]	12.3 ± 0.1 [a]	10.2 ± 0.1 [a]	2.0	0.0030	3.3
FC-25	β′-2L	42.1 ± 0 [a]	12.7 ± 0.2 [a]	10.6 ± 0.3 [a]	2.2	0.0021	3.3
SC-25	β′-2L	42.1 ± 0 [a]	11.5 ± 0.5 [a]	9.6 ± 0.5 [a]	2.2	0.0021	3.3

Slow Cooling of PO to 20 °C

For SC-20, slightly before reaching 20 °C (at about 49 min), crystallization starts, as shown by the formation of the α peak at q = 1.51 $Å^{-1}$ (Figure 3E, blue). As such, a decrease in the cooling rate did not change the preferred nucleation polymorph toward a more stable one [26]. At the mesoscale, the bending sections at low and high q are immediately more pronounced compared to FC-20 (Figure 3F,G, blue). Upon α growth, both bending sections shift toward lower q, indicating CNP and aggregate growth (Figure 3F,G, green). After 56 min, a shift toward q = 1.44, 1.49, 1.55, and 1.61 $Å^{-1}$ follows (Figure 3E, pink), representing the α to β′ transformation. As such, the lifespan of the dominant α polymorphic phase is shorter in a PO sample that was cooled at 1 °C/min compared to 20 °C/min. This might be related to the amount of α polymorph at the beginning of crystallization (nucleation). When the polymorphic transition is completed (62 min), the second bending section seems to have disappeared (Figure 3G, pink). This might be due to the fact that the sizes encountered for the aggregates are above the probing limit of USAXS (2 μm), which is consistent with the appearance of the crystallites in cryo-SEM (Figure 1F). After one hour of isothermal crystallization, the slope at high q amounts to 3.3. This is slightly lower than for FC-20. This

difference can, however, not be validated, as visualization of the CNPs requires de-oiling. The cut-off is found at q = 0.0035 $Å^{-1}$, indicating that the SC-20 CNPs will be bigger than those found for FC-20. This is in line with the observations of Peyronel (2013, 2014) for a 20% SSS or 20% PPP in an OOO sample cooled at 0.5 °C/min and 30 °C/min [18,38]. Acevedo et al. (2011) applied TEM analysis to a 1/1 FHCO/HOSO sample and found that all the CNP dimensions were bigger when crystallizing at 1 °C/min compared to 10 °C/min [47]. The straight section at low q decays to the power 2, which is consistent with the platelet shape as discussed for FC-20.

Fast Cooling of PO to 25 °C

For FC-25, crystallization only starts from 11 min onwards (Figure 3I, blue), which is later than the timing found with PLM and DSC (Figures A2 and A3, Appendix A) and might be related to the low amount of solid fat, which complicates the reading of the WAXS/USAXS curves. A small peak at q = 1.51 $Å^{-1}$ is found, which is consistent with the formation of the α polymorph. Although stated in the literature that for some PO the melting point of the α polymorph is below 25 °C [14], this study shows a clear transition from the α polymorph to the β′ polymorph. Figure 3J shows that the overall shape of the USAXS curve is different from FC-20 and SC-20. It is clear that the bend is not pronounced at all. This might be explained by the low amount of solids, their low scattering power, and the expected high polydispersity. The curves are clearer when checking the $I \times q^2$ and $I \times q^4$ graphs (Figure 3K,L). For FC-25, the bending section seems situated toward lower q compared to FC-20 and SC-20. As such, the CNPs are expected to be larger. As is the case for the other samples, a clear aggregation level is present, as long as α crystals persist. After half an hour, four WAXS peaks replace the α peak: q = 1.44, 1.49, 1.56, and 1.62 $Å^{-1}$ (Figure 3I, pink). These peaks, characteristic of the β′ polymorph, are prevalent until the end of the isothermal time (Figure 3I, red). The polymorphic transition corresponds to the formation of a fanning crown around the dense centers in PLM (Figure A2, Appendix A). In USAXS, the bending at higher q shifts toward lower q (Figure 3J, pink).

After one hour of isothermal crystallization (Figure 3J, red), the curve is characterized by decay to the powers of 2.2 and 3.4 for low and high q, respectively. These values indicate equally a platelet-like shape and a similar interface contrast. The cut-off is found at 0.0025 $Å^{-1}$, indicating larger CNPs than for the samples crystallized at 20 °C. Although the dense center remains present in the PLM images after one hour of isothermal time (Figure 1), WAXS does not present evidence of a persistent α phase (Figure 3I, red), as was suggested earlier [28].

Slow Cooling of PO to 25 °C

For SC-25 (Figure 3M–P), profiles comparable to FC-25 are found, comprising an unclear first bend and a more pronounced second bend at the beginning of crystallization (Figure 3N–P, blue). Again, the slower cooling rate seems to result in a more pronounced profile at lower q, implying that more order in the arrangements can be created by a slower driving force for cooling. The bend at high q shifts toward lower q over time, while the second bend gets lost (Figure 3O). Nonetheless, with a slower cooling rate, the profile found after one hour of crystallization is fairly similar to FC-25.

When comparing the results after one hour of isothermal crystallization (Table 2), the samples crystallized under different conditions all show the predominant presence of the β′ polymorph. Despite the differences in the cooling rate and isothermal temperature, the most stable polymorph (β) was not observed. It has been reported that it can be formed in PO; for example, at very low cooling rates or after prolonged storage [3,13].

On the mesoscale, USAXS analysis confirmed the platelet-like shape of the CNPs for all conditions with the presence of similar slopes of a power of −2 in the middle q region. It is found that FC-20 has the smallest CNP and probably the smallest aggregate based on the position of the cut-off points. For SC-20, FC-25, and SC-25, no evidence for aggregation was found within the USAXS range (<2 μm). The lower cooling rate applied in SC-20 compared

to FC-20 creates bigger CNPs. The CNPs formed at 25 °C were the biggest, with no clear effect of the cooling rate.

3.2.2. SAXS

SAXS serves to assess the chain length structure of TGs, i.e., the distance between the methyl end groups of FAs that are part of the opposite TGs and is often referred to as the double (2L) or triple (3L) confirmation. For lamellar structures, several equally spaced SAXS peaks can be found (den Adel et al., 2018) [24]. Figure 5 shows the time-resolved crystallization obtained by SAXS, focusing on the first-order (001) SAXS peak. As long as only oil is present, the studied SAXS region shows a fairly flat profile.

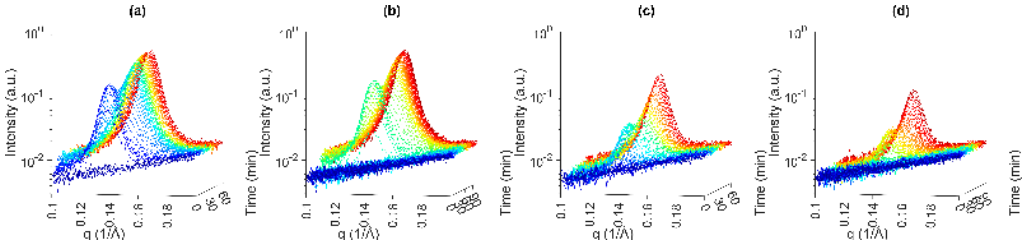

Figure 5. Time-resolved SAXS profiles for FC-20 (**a**), SC-20 (**b**), FC-25 (**c**), and SC-25 (**d**). Colors from dark blue to dark red represent the evolution in time per condition.

Fast Cooling of PO to 20 °C

For FC-20, right after reaching 20 °C, like the α peak in WAXS, a first peak becomes prevalent at q = 0.137 $Å^{-1}$ (d = 45.9 Å), suggesting a 2L configuration [48]. The intensity of the peak increases until 8 min. Then, peak intensity slightly decreases, and the peak widens to the right, simultaneously with the polymorphic transition found in WAXS. From 15 min onwards, the new peak is centered around q = 0.149 $Å^{-1}$ (d = 42.1 Å), timewise corresponding with the β′ peak. Hence, β′ crystals also have a 2L packing, but the perpendicular length is slightly different due to the tilt of the lamellae. The value of d_{001} = 42.3 Å (Table 2) was found to be specific for fats containing PPP [3]. The β′-2L peak intensity continues to increase, implying that additional β′-2L crystallization is happening and suggesting that crystallization was not yet finalized after one hour at 20 °C.

Slow Cooling of PO to 20 °C

As shown in Figure 5, the time-resolved SAXS profile found for SC-20 resembles the one for FC-20. Crystallization starts right before the end of the cooling period. A peak at q = 0.137 $Å^{-1}$ shows an α-2L longitudinal spacing of 45.9 Å. From 56 min onwards, the maximum intensity starts to drop, caused by the formation of a second peak centered at q = 0.149 $Å^{-1}$ (d_{001} = 42.1 Å). The peak center positions (d_{001}) found for FC-20 and SC-20 follow equal trends, which is to be expected as it is supposed the same, and TGs will crystallize, as the isothermal temperature is similar.

Fast Cooling of PO to 25 °C

The SAXS profile found for FC-25 in Figure 5 is more scattered, and lower overall peak intensities are reached due to the lower amount of fat that crystallizes at 25 °C compared to 20 °C. Crystallization starts at around 11 min, with a small peak appearing around q = 0.138 $Å^{-1}$ at the same time as the α polymorph. Hence, the α crystals show a 2L longitudinal packing with d = 45.5 Å, which is about 0.4 Å shorter than the α-2L found for FC-20. From 22 min onwards, the peak center starts to shift toward q = 0.149 $Å^{-1}$, corresponding with 2L (d_{001} = 42.1 Å). Again, the shift in 2L distance goes along with the transition toward crystallization in the β′ polymorph, as seen in WAXS. The β′-2L peak remains to grow in intensity until the end of the one hour of isothermal time, showing intensities well beyond the maximum intensity found for α peak. Compared to FC-20 and SC-20, it is clear that fewer α-2L crystals were formed (Figure 5).

Slow Cooling of PO to 25 °C

For SC-25, a similar profile to FC-25 was found with an α-2L peak centered around q = 0.138 $Å^{-1}$ prevalent from 56 min and a β′-2L peak at q = 0.149 $Å^{-1}$, which was dominant from 81 min onwards.

Overall, it can be concluded that after one hour of isothermal time, the polymorphic form and longitudinal spacing for each of the applied cooling protocols is the same (β′-2L). The 2L form is most common for PO; 3L is only formed at very specific cooling temperatures [7]. The lamellar spacing (d_{001}) of α-2L at 25 °C is slightly lower than for 20 °C, showing the crystallization of a slightly shorter fraction of FA/TGs.

Average Thickness and Thickness Distribution of CNPs

The Scherrer equation was applied to estimate the average size of the thickness of the CNPs. An average of 12.0 ± 0.1 [a], 12.3 ± 0.1 [a], 12.7 ± 0.2 [a], and 11.5 ± 0.5 [a] was found for FC-20, SC-20, FC-25, and SC-25 (Table 2). This results for all samples in similar average domain sizes of approximately 500 Å. The domain size is assumed to be the smallest dimension of the CNP. The BWA method provides a distribution of the number of lamellae making up the CNPs. As such, it serves as an assessment of the heterogeneity of the CNP thicknesses making up the solid fat and is more informative than the Scherrer equation. Figure 6 shows the volume-weighted number of lamellae distributions for FC-20, SC-20, FC-25, and SC-25 after one hour of isothermal time and their cumulative counterpart. A broad distribution was found for all protocols after one hour of isothermal crystallization, resulting in domain sizes of 127 to 1013 Å. As these results come from lab-scale SAXS data, which is prone to peak broadening, it is assumed that the actual numbers will be slightly higher. The number of lamellae range from 3 to 24. The start and end points of the distribution are narrower than the limits that were provided to the BWA method (0–30 lamellae). The volume-weighted average value of the distributions is similar for all cooling protocols: 10.1 [a] ± 0.1, 10.2 [a] ± 0.1, 10.6 [a] ± 0.3, and 9.6 [a] ± 0.5 for, respectively, FC-20, SC-20, FC-25, and SC-25 (Table 2). The average trends seen by the BWA method are thus similar to those found by the Scherrer equation. The number found by the BWA method is smaller, as found by den Adel et al. (2018) and Rondou et al. (2022) [2,24]. After one hour of isothermal crystallization, around 60% of the CNPs consist of 3–10 lamellae and about 40% of 11–20 lamellae. As such, we can conclude that this analysis unravels the wide variety of thicknesses present within the CNPs of one cooling protocol. Despite the fact that USAXS analysis suggests differences in the overall CNP size under the different cooling protocols, the thickness of the CNP (smallest dimension) is similar for all samples. A comparable result was obtained by Acevedo et al. (2011), where slowly cooled FHCO/HOSO 1/1 resulted in clearly longer and wider CNPs than the fast-cooled sample, but the thicknesses remained similar [47].

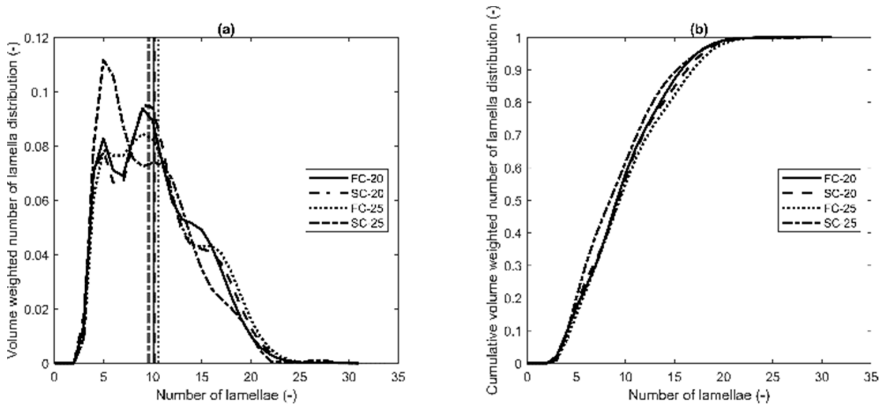

Figure 6. Volume-weighted crystallite thickness distribution curves (**a**) and their cumulative counterpart (**b**) as a function of the number of lamellae obtained by the BWA method after one hour of isothermal crystallization. Vertical lines indicate the volume-weighted mean number of lamellae.

4. Conclusions

It is shown in this work that both the cooling rate (FC and SC) and isothermal temperature (20 or 25 °C) affect the size and morphology of the fat crystal network on the micro- and mesoscale. The coldest temperature and the highest cooling rate, which generated the highest driving force for crystallization, resulted in a network consisting of small flocs made from small CNPs and small crystallites. Slower cooling resulted in larger CNPs and a snowflake-like fat crystal network, while a higher temperature resulted in the formation of separated crystal flocs, consisting of a dense saturated center and surrounded by a fanning crown. Cryo-SEM was found to be a useful technique to visualize the fat crystal flocs after oil extraction but could not resolve sufficiently single CNPs. For FC-20 and SC-20, a clear network structure with entangled flocs was found, while for FC-25 and SC-25, more separate flocs were seen, probably due to de-oiling. In contrast to the smooth surface of FC-20 and SC-20 flocs after de-oiling, the FC-25 and SC-25 flocs showed the presence of petal-like aggregates of crystallites on the surface. Raman spectroscopy unraveled that for FC-25 and SC-25, a center is present within the flocs consisting of high amounts of PPP compared to its surroundings. The high PPP (and other saturated TGs) content in the center is confirmed by the high PPP retention upon oil extraction with isobutanol.

Despite the application of different cooling protocols, all samples showed a similar polymorphic behavior (nanoscale) with the formation of the α polymorph and a transition to the β′ polymorph, which was the stable end polymorph within the timeframe of the experiment. SAXS analysis revealed similar longitudinal spacings, showing a 2L conformation for all samples. In addition, the BWA method illustrated that for all conditions, CNPs consist of three to twenty-four lamellae, approximately 60% three to ten lamellae and 40% eleven to twenty lamellae. A comparison of the changes in USAXS and WAXS unraveled that the changes on the nano- and mesoscale are related. In comparison to the established TEM techniques, it was shown here, by applying time-resolved USAXS analysis, that α CNPs were smaller than β′ CNPs and that CNPs grow during crystallization. The presence of a complete second level (aggregation) was only detected along with α crystals, while during the polymorphic transition, the intensity at lower q seemed to decrease, removing the second level from the measured q-range probably due to an increase in the size of the aggregates. Despite the similar nanoplatelet thickness found by BWA, after one hour of isothermal crystallization at 20 or 25 °C, the USAXS cut-off position was similar for FC-25 and SC-25 but clearly different for FC-20 and SC-20. The scatterer size was estimated to be the biggest for FC-25 and SC-25, followed by SC-20 and, lastly, FC-20. The scatterer shape (platelet), as visualized by TEM, was confirmed by USAXS for all samples.

The current study showed that it is possible to apply USAXS to study fat samples during crystallization in situ without the need for sample preparation. Moreover, it was shown that both the cooling rate and isothermal temperature affect the micro- and mesoscale. Special attention is required to study the complementarity of USAXS and microscopy investigations. This highlights the need for further scientific investigation to understand the structural build-up of the fat crystal network, especially for more complex systems, such as fat blends and suspensions. In addition, it will be important to investigate the fat crystal network at the full-length scale in relation to its functionality in order to strive toward tailoring the fat crystal network for specific product functionalities. In the long term, the fundamental understanding of the effect of processing on fat crystallization will help to improve the technological functionality and sensory properties of multiple food products.

Author Contributions: Conceptualization, K.M., D.A.T.-S., D.V.d.W., F.V.B. and K.D.; methodology, F.D.W., I.A.P. and K.R.; formal analysis, F.D.W., K.R. and B.L.; investigation, F.D.W. and I.A.P.; resources, D.A.T.-S.; data curation, F.D.W.; writing—original draft, F.D.W.; writing—review and editing, F.D.W., I.A.P., K.R., K.M., D.A.T.-S., D.V.d.W., F.V.B., A.G.S. and K.D.; visualization, F.D.W.; supervision, K.M., D.A.T.-S., D.V.d.W., F.V.B., A.G.S. and K.D.; project administration, D.A.T.-S., F.V.B., A.G.S. and K.D.; funding acquisition, K.M., D.A.T.-S., D.V.d.W., F.V.B. and K.D. All authors have read and agreed to the published version of the manuscript.

Funding: This research was funded by the FLANDERS RESEARCH FUND (FWO), grant number 1128923N (scholarship), 1SA5321N (scholarship), AUGE09/29 (Hercules Grant cryo-SEM equipment), and AUGE/17/29 (Hercules Grant XRS equipment) and I002600N.

Data Availability Statement: The data presented in this study are openly available in Zenodo at 10.5281/zenodo.10370349, reference number 10370349. Raw USAXS and WAXS data are available via the European Synchrotron Radiation Facility: 10.15151/ESRF-DC-1469057171.

Acknowledgments: We are grateful to Corine Loijson and Joost Coudron (Vandemoortele Lipids) for their assistance with the TG fat analysis. We acknowledge the European Synchrotron Radiation Facility for the provision of synchrotron radiation facilities, and we would like to thank Theyencheri Narayanan and William Chevremont for their assistance with using beamline ID02. TEM analyses were performed at the UGent TEM Core Facility.

Conflicts of Interest: The authors declare no conflicts of interest.

Appendix A

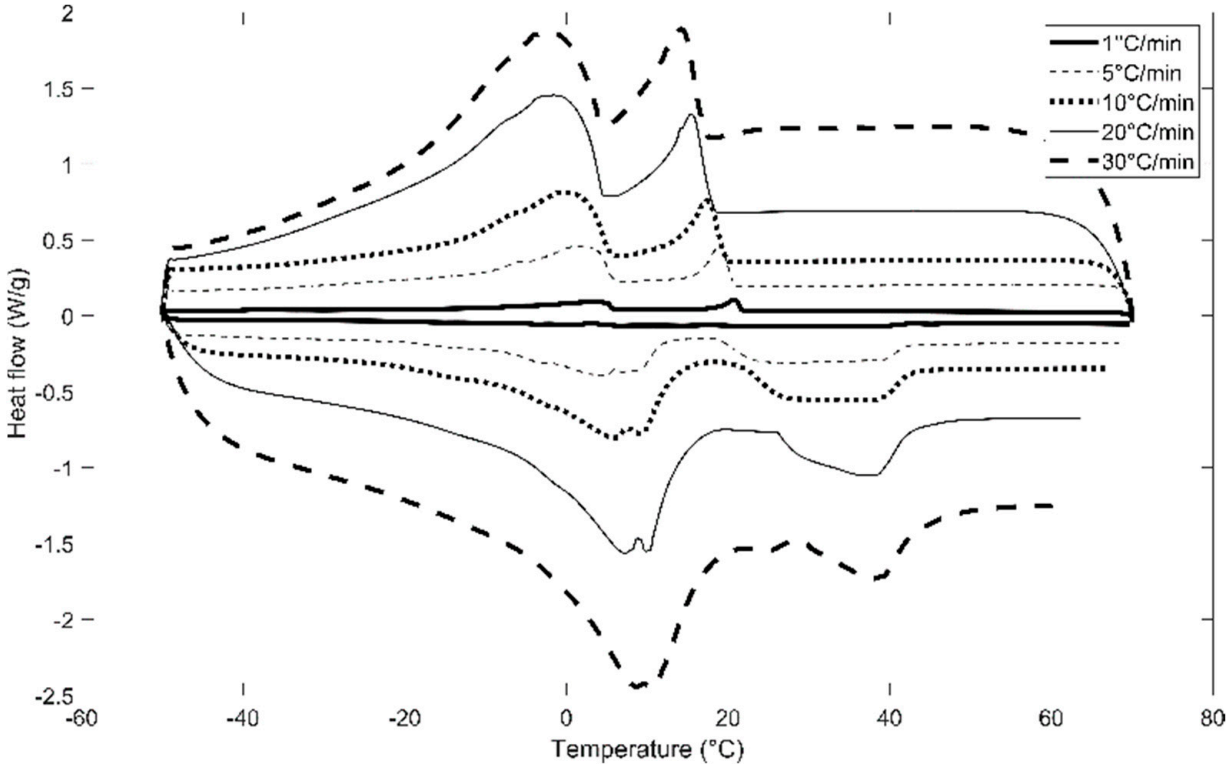

Figure A1. Crystallization and subsequent melting of PO at different cooling/heating rates. Although measurements are executed in triplicate, this graph represents one exemplary curve, as there is little variation between the repetitions.

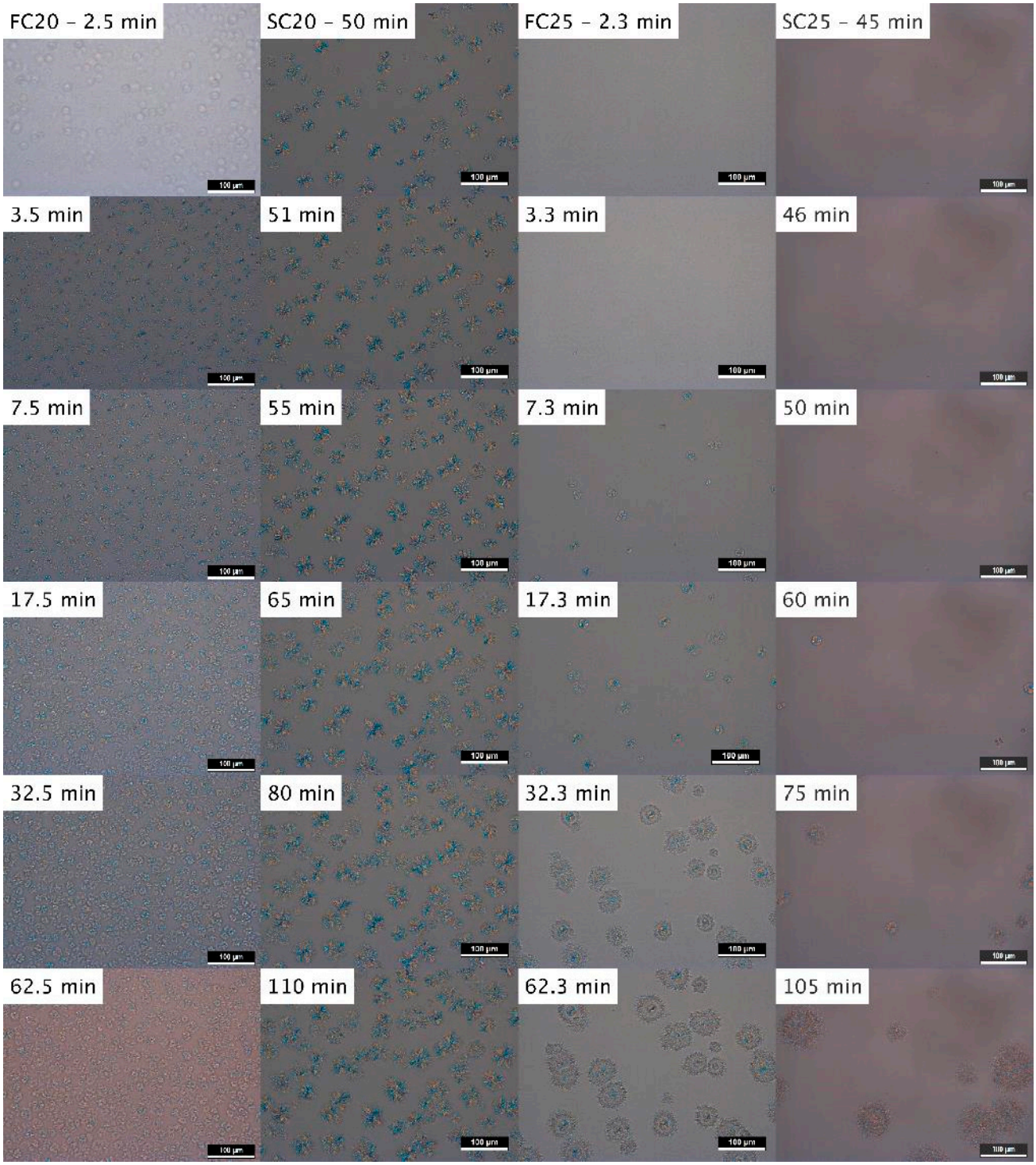

Figure A2. Time-resolved PLM images. From left to right: FC-20, SC-20, FC-25, and SC-25. Timing is specified from the start of cooling. Per row, this corresponds to 0, 1, 5, 15, 30, and 60 min of isothermal time.

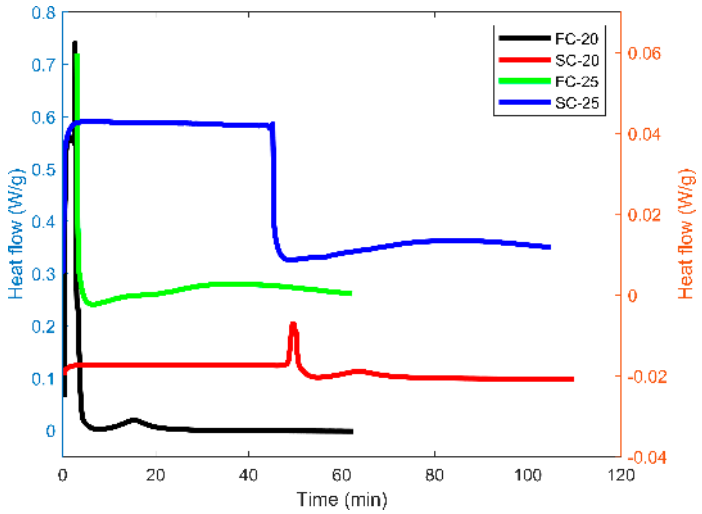

Figure A3. Thermogram of heat flow as a function of time measured with differential scanning calorimetry during cooling and subsequent 1 h of isothermal time. FC-20 and SC-20 are represented on the left y-axis, and FC-25 and SC-25 are represented on the right y-axis. Data are vertically shifted for readability.

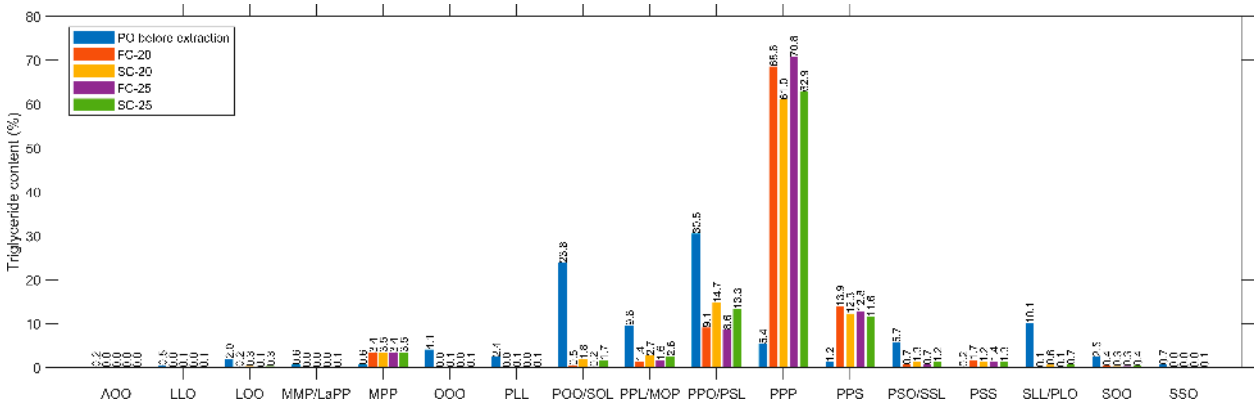

Figure A4. Overview of TG content before (PO) and after extraction (FC-20, FC-25, SC-20, and SC-25).

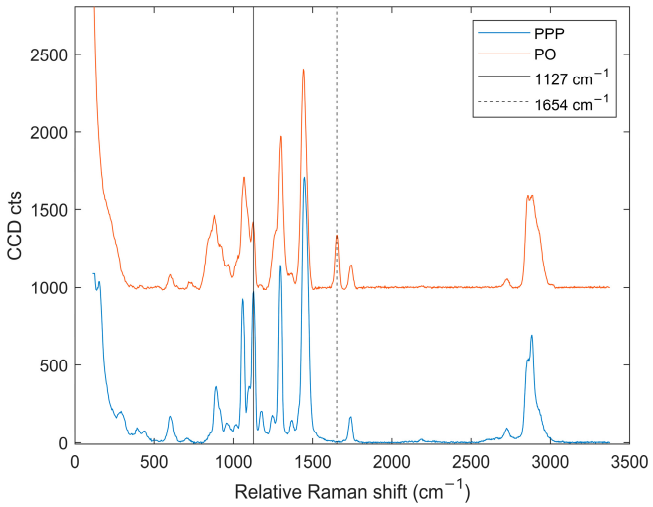

Figure A5. Raman spectra for PPP and PO (average of 10 measurements of 0.5s). Data are vertically shifted for readability. Vertical lines indicate the Raman shifts selected for solid fat (1127 cm^{-1}) and oil (1654 cm^{-1}).

References

1. Aini, I.N.; Miskandar, M.S. Utilization of palm oil and palm products in shortenings and margarines. *Eur. J. Lipid Sci. Tech.* **2007**, *109*, 422–432. [CrossRef]
2. Rondou, K.; De Witte, F.; Van Bockstaele, F.; Dewettinck, K. Microstructure development in semi-liquid shortenings upon storage. *J. Am. Oil Chem. Soc.* **2022**, *99*, 57.
3. Sato, K. *Polymorphic Properties of Palm Oil and Its Major Component Triacyglycerols*; AOCS Press: Champaign, IL, USA, 2012; pp. 393–429.
4. Macias-Rodriguez, B.; Marangoni, A.G. Rheological characterization of triglyceride shortenings. *Rheol. Acta* **2016**, *55*, 767–779. [CrossRef]
5. Bayés-García, L.; Calvet, T.; Cuevas-Diarte, M.; Ueno, S.; Sato, K. Crystallization and transformation of polymorphic forms of trioleoyl glycerol and 1,2-dioleoyl-3-rac-linoleoyl glycerol. *J. Phys. Chem. B* **2013**, *117*, 9170–9181. [CrossRef] [PubMed]
6. Bayés-García, L.; Calvet, T.; Cuevas-Diarte, M.À.; Ueno, S.; Sato, K. Heterogeneous microstructures of spherulites of lipid mixtures characterized with synchrotron radiation microbeam X-ray diffraction. *Cryst. Eng. Comm.* **2011**, *13*, 6694–6705. [CrossRef]
7. Sainlaud, C.; Tache, O.; Testard, F.; Saiter, J.M.; Bohin, M.C.; Coquerel, G. Impact of Cooling Profile on Refined Palm Oil Crystallization: Microscopic and Small and Wide-Angle X-Ray Scattering Investigations. *Eur. J. Lipid Sci. Tech.* **2022**, *124*, 2100045. [CrossRef]
8. Marangoni, A.; Acevedo, N.; Maleky, F.; Co, E.; Peyronel, F.; Mazzanti, G.; Quinn, B.; Pink, D. Structure and functionality of edible fats. *Soft Matter* **2012**, *8*, 1275–1300. [CrossRef]
9. Mishra, K.; Kummer, N.; Bergfreund, J.; Kampf, F.; Bertsch, P.; Pauer, R.; Nystrom, G.; Fischer, P.; Windhab, E.J. Controlling lipid crystallization across multiple length scales by directed shear flow. *J. Colloid Interface Sci.* **2023**, *630*, 731–741. [CrossRef]
10. Tang, D.; Marangoni, A.G. Quantitative study on the microstructure of colloidal fat crystal networks and fractal dimensions. *Adv. Colloid Interface Sci.* **2006**, *128–130*, 257–265. [CrossRef] [PubMed]
11. Omar, Z.; Hishamuddin, E.; Sahri, M.M.; Fauzi, S.H.M.; Dian, N.L.H.M.; Ramli, M.R.; Abd Rashid, N. Palm Oil Crystallisation: A Review. *J. Oil Palm Res.* **2015**, *27*, 97–106.
12. Zaliha, O.; Chong, C.L.; Cheow, C.S.; Norizzah, A.R.; Kellens, M.J. Crystallization properties of palm oil by dry fractionation. *Food Chem.* **2004**, *86*, 245–250. [CrossRef]
13. Nguyen, V.; Rimaux, T.; Truong, V.; Dewettinck, K.; Van Bockstaele, F. Granular Crystals in Palm Oil Based Shortening/Margarine: A Review. *Cryst. Growth Des.* **2020**, *20*, 1363–1372. [CrossRef]
14. De Graef, V. *Microstructural Properties of Isothermal Palm Oil Crystallization*; Ghent University: Ghent, Belgium, 2009.
15. Peyronel, F.; Pink, D.A. Chapter 9-Ultra-Small Angle X-ray Scattering: A Technique to Study Soft Materials. In *Structure-Function Analysis of Edible Fats*, 2nd ed.; Marangoni, A.G., Ed.; AOCS Press: Champaign, IL, USA, 2018; pp. 267–285.
16. Peyronel, F.; Pink, D. Using USAXS to Predict the Under-tempered Chocolate Microstructure. *J. Am. Oil Chem. Soc.* **2021**, *98*, 56.
17. Peyronel, F.M.; Pink, D.A. The nano-to meso-scale solid structure of edible fats as seen by USAXS: Static versus dynamics results. In Proceedings of the 7th International Symposium on Food Rheology and Structure, Zurich, Switzerland, 10 June 2015.
18. Peyronel, F.; Ilavsky, J.; Mazzanti, G.; Marangoni, A.G.; Pink, D.A. Edible oil structures at low and intermediate concentrations. II. Ultra-small angle X-ray scattering of in situ tristearin solids in triolein. *J. Appl. Phys.* **2013**, *114*, 234902. [CrossRef]
19. Nikolaeva, T.; Adel, R.D.; Velichko, E.; Bouwman, W.G.; Hermida-Merino, D.; As, H.V.; Voda, A.; Duynhoven, J.V. Networks of micronized fat crystals grown under static conditions. *Food Funct.* **2018**, *9*, 2102–2111. [CrossRef] [PubMed]
20. Narayanan, T.; Sztucki, M.; Zinn, T.; Kieffer, J.; Homs-Puron, A.; Gorini, J.; Van Vaerenbergh, P.; Boesecke, P. Performance of the time-resolved ultra-small-angle X-ray scattering beamline with the Extremely Brilliant Source. *J. Appl. Crystallogr.* **2022**, *55*, 98–111. [CrossRef] [PubMed]
21. Patterson, A.L. The Scherrer Formula for X-Ray Particle Size Determination. *Phys. Rev.* **1939**, *56*, 978–982. [CrossRef]
22. Scherrer, P. Bestimmung der Größe und der inneren Struktur von Kolloidteilchen mittels Röntgenstrahlen. *Nachrichten Ges. Wiss. Göttingen Math. Phys. Kl.* **1918**, *1918*, 98–100.
23. Acevedo, N.C.; Marangoni, A.G. Characterization of the Nanoscale in Triacylglycerol Crystal Networks. *Cryst. Growth Des.* **2010**, *10*, 3327–3333. [CrossRef]
24. den Adel, R.; van Malssen, K.; van Duynhoven, J.; Mykhaylyk, O.O.; Voda, A. Fat Crystallite Thickness Distribution Based on SAXD Peak Shape Analysis. *Eur. J. Lipid Sci. Tech.* **2018**, *120*, 1800222. [CrossRef]
25. Ramel, P.R.R.; Peyronel, F.; Marangoni, A.G. Characterization of the nanoscale structure of milk fat. *Food Chem.* **2016**, *203*, 224–230. [CrossRef] [PubMed]
26. Sato, K.; Bayés-García, L.; Calvet, T.; Cuevas-Diarte, M.À.; Ueno, S. External factors affecting polymorphic crystallization of lipids. *Eur. J. Lipid Sci. Tech.* **2013**, *115*, 1224–1238. [CrossRef]
27. Smith, P.; Shiori, T.; Hondoh, H.; Wallecan, J.; Ueno, S. Polymorphic and microstructural behaviors of palm oil/lecithin blends crystallized under shear. *J. Am. Oil Chem. Soc.* **2022**, *99*, 665–674. [CrossRef]
28. Chen, C.W.; Lai, O.M.; Ghazali, H.M.; Chong, C.L. Isothermal crystallization kinetics of refined palm oil. *J. Am. Oil Chem. Soc.* **2002**, *79*, 403–410. [CrossRef]
29. Herrera, M.L.; Hartel, R.W. Effect of processing conditions on crystallization kinetics of a milk fat model system. *J. Am. Oil Chem. Soc.* **2000**, *77*, 1177–1188. [CrossRef]

30. Campos, R.; Narine, S.S.; Marangoni, A.G. Effect of cooling rate on the structure and mechanical properties of milk fat and lard. *Food Res. Int.* **2002**, *35*, 971–981. [CrossRef]
31. Chawla, P.; deMan, J.M.; Smith, A.K. Crystal Morphology of Shortenings and Margarines. *Food Struct.* **1990**, *9*, 2.
32. Berry, S. Triacylglycerol structure and interesterification of palmitic and stearic acid-rich fats: An overview and implications for cardiovascular disease. *Nutr. Res. Rev.* **2009**, *22*, 3–17. [CrossRef]
33. Toro-Vazquez, J.; Dibildox-Alvarado, E.; Herrera-coronado, V. Triacylglyceride crystallization in vegetable oils: Application of models, measurements, and limitations. *Cryst. Solidif. Prop. Lipids* **2001**, *8*, 53–78.
34. Bresson, S.; El Marssi, A.; Khelifa, B. Raman spectroscopy investigation of various saturated monoacid triglycerides. *Chem. Phys. Lipids* **2005**, *134*, 119–129. [CrossRef]
35. Czamara, K.; Majzner, K.; Pacia, M.Z.; Kochan, K.; Kaczor, A.; Baranska, M. Raman spectroscopy of lipids: A review. *J. Raman Spectrosc.* **2015**, *46*, 4–20. [CrossRef]
36. Glatter, O. Chapter 6-Contrast Variation. In *Scattering Methods and Their Application in Colloid and Interface Science*; Glatter, O., Ed.; Elsevier: Amsterdam, The Netherlands, 2018; pp. 111–121.
37. Peyronel, F. Ultra Small Angle X-Ray Scattering Studies of Triacylglycerol Crystal Networks. Ph.D. Thesis, University of Guelph, Guelph, ON, Canada, 2014.
38. Hammouda, B. A new Guinier-Porod model. *J. Appl. Crystallogr.* **2010**, *43*, 716–719. [CrossRef]
39. Beaucage, G. Approximations Leading to a Unified Exponential/Power-Law Approach to Small-Angle Scattering. *J. Appl. Crystallogr.* **1995**, *28*, 717–728. [CrossRef]
40. Beaucage, G. Small-Angle Scattering from Polymeric Mass Fractals of Arbitrary Mass-Fractal Dimension. *J. Appl. Crystallogr.* **1996**, *29*, 134–146. [CrossRef]
41. Matsui, K.; Kamigaki, T.; Wakui, R.; Nishino, Y.; Ito, Y.; Miyazawa, A.; Yoshioka, K.; Shiota, M. Evaluation of crystal nanoplatelet aggregation in intact butter by atomic force microscopy. *LWT* **2021**, *140*, 110801. [CrossRef]
42. Porod, G. Die Röntgenkleinwinkelstreuung von dichtgepackten kolloiden Systemen. II. Teil. *Kolloid-Z.* **1952**, *125*, 108–122. [CrossRef]
43. Mazzanti, G. Prenucleation Structuring in Liquid Triacylglycerols: Navigating a Non-ideal Landscape. *J. Am. Oil Chem. Soc.* **2021**, *98*, 60.
44. Yap, P.H.; de Man, J.M.; de Man, L. Polymorphism of palm oil and palm oil products. *J. Am. Oil Chem. Soc.* **1989**, *66*, 693–697. [CrossRef]
45. Roe, R.J. Methods of X-ray and Neutron Scattering in Polymer Science. *Soft Matter* **2000**, *54*, 60–61.
46. Glatter, O. Chapter 2-General Theorems and Special Cases. In *Scattering Methods and their Application in Colloid and Interface Science*; Glatter, O., Ed.; Elsevier: Amsterdam, The Netherlands, 2018; pp. 19–32.
47. Acevedo, N.C.; Peyronel, F.; Marangoni, A.G. Nanoscale structure intercrystalline interactions in fat crystal networks. *Curr. Opin. Colloid Interface Sci.* **2011**, *16*, 374–383. [CrossRef]
48. Mazzanti, G.; Marangoni, A.G.; Idziak, S.H.J. Modeling phase transitions during the crystallization of a multicomponent fat under shear. *Phys. Rev. E* **2005**, *71*, 041607. [CrossRef] [PubMed]